Article

Sideband Vibro-Acoustics Suppression and Numerical Prediction of Permanent Magnet Synchronous Motor Based on Markov Chain Random Carrier Frequency Modulation

Yong Chen [1,2,*], Bingxiao Yan [1,2], Liming Zhang [3], Kefu Yao [4] and Xue Jiang [1,2]

1   State Key Laboratory of Featured Metal Materials and Life-Cycle Safety for Composite Structures, Guangxi University, Nanning 530004, China; ybx20001@163.com (B.Y.); jx1109017224@163.com (X.J.)
2   New Energy Automotive Research Center, School of Mechanical Engineering, Guangxi University, Nanning 530004, China
3   Wuhan Fareo Automotive Parts Co., Ltd., Wuhan 430090, China; zlm97924@163.com
4   Dongfeng Liuzhou motor Co., Ltd., Liuzhou 545005, China; yaokf@dflzm.com
*   Correspondence: chenyong1585811@163.com

Abstract: This paper presents a Markov chain random carrier frequency modulation (MRCFM) technique for suppressing sideband vibro-acoustic responses caused by discontinuous pulse-width modulation (DPWM) in permanent magnet synchronous motors (PMSMs) for new energy vehicles. Firstly, the spectral and order distributions of the sideband current harmonics and radial electromagnetic forces introduced by DPWM are characterized and identified. Then, the principle and implementation method of three-state Markov chain random number generation are proposed, and particle swarm optimization (PSO) algorithm is chosen to quickly find the key parameters of transition probability and random gain. A Simulink and JMAG multi-physics field co-simulation model is built to simulate and predict the suppression effect of the MRCFM method on the sideband vibro-acoustic response. Finally, a 12-slot-10-pole PMSM test platform is built for experimental testing. The results show that the sideband current harmonics and vibro-acoustic response are effectively suppressed after the optimization of Markov chain algorithm. The constructed multi-physics field co-simulation model can accurately predict the amplitude characteristics of the sideband current harmonics and vibro-acoustic response.

Keywords: permanent magnet synchronous motor; Markov chain random carrier frequency modulation; multi-physics field co-simulation model; sideband current harmonic; vibro-acoustics control; discontinuous pulse-width modulation

1. Introduction

In recent years, by virtue of their high efficiency, high reliability and superior speed regulation performance, permanent magnet synchronous motors (PMSMs) have been widely used in the development of new energy vehicles [1,2]. The drive system of a PMSM typically uses the voltage source inverter (VSI) as the hardware-based control system [3]. However, the VSI drive makes the motor line voltage and phase current rich in harmonic components [4,5]. Usually, conventional pulse-width modulation (PWM) techniques employ fixed carrier frequency modulation, resulting in the sideband harmonic current spectrum concentrated in the carrier frequency and its multiples [6–8], thereby causing a high-frequency, uncomfortable "whistling" radiated from the motor [9], presenting a challenge to the vehicle's noise, vibration and harshness (NVH) performance [10].

In order to effectively suppress the harmonic components of sidebands, many scholars, both domestic and abroad, have conducted research on optimizing the harmonic current of the inverter. Cassat et al. [11] analyzed the current's harmonic characteristics introduced by PWM and derived the corresponding analytical model of radial electromagnetic force.

Tsoumas et al. [12] investigated the basic characteristics of on-line and off-line PWM techniques and their effects on the electromagnetic noise of motors, validating the accuracy of the theoretical analysis through experiments under variable speed conditions. Schulz et al. [13] proposed a method for implementing variable-delay random pulse-width modulation in automotive traction drive inverters, which can reduce electromagnetic radiation from the inverter and minimize electromagnetic compatibility filtering to decrease the noise generated by the drive system. Zhang et al. [14] proposed a new method of combining a dual three-phase PMSM with a carrier phase-shift mechanism to substantially reduce the odd-order PWM frequency vibration. Xu et al. [15] analyzed the effects of spread spectrum modulation based on sinusoidal waves. Although the periodic spread spectrum modulation technique allows the originally fixed carrier frequency to be varied in a deterministic and controllable manner, the sideband harmonic suppression is limited. Qiu et al. [16] analyzed the relationship between sideband current harmonics and mechanical vibration noise in different carrier frequency domains, which provides a theoretical foundation for the prediction of the vibro-acoustics of PMSMs.

However, the studies on current harmonics and the vibro-acoustic response are mostly based on continuous pulse-width modulation (CPWM) [17,18], and the characteristic laws of sideband harmonics generated by the DPWM strategies are not yet well studied. The DPWM can significantly improve the inverter efficiency and has been widely applied in high-power voltage source inverters [19,20], but it produces richer sideband harmonic components. Despite its effectiveness in suppressing sideband harmonic components, random carrier frequency modulation (RCFM) has a flaw when it comes to total harmonic distortion [21]. Conventional RCFM techniques usually employ pseudo-random number generation methods based on the use of linear congruence or look-up table methods [22]. Compared with ideal random numbers, pseudo-random numbers may be larger than or smaller than the mathematical expectation within local time periods, which results in the generated randomized carrier frequency being successively larger or smaller than the initial carrier frequency [23]. This imbalance will not maximize the suppression of sideband harmonics to further suppress the sideband vibro-acoustics [24–26], and it will result in large current ripples in the output signal of the system, thereby causing output torque fluctuations and the generation of additional switching losses [27].

To this end, this paper proposes a Markov chain random carrier frequency modulation (MRCFM) technique to promote the inhibitory effect of sideband harmonic current and vibration noise. Firstly, the sideband current harmonics and radial electromagnetic force introduced by the DPWM are characterized and analyzed. The MRCFM approach aims to improve the DPWM strategy by utilizing the three-state Markov chain algorithm and integrating it with the PSO algorithm for random parameter optimization. Secondly, a multi-physics co-simulation model is established to simulate and predict the suppression effect of the MRCFM approach on sideband vibro-acoustic response. The vibro-acoustic response of the experimental prototype is calculated based on the modal superposition and complete integration method. Finally, the validity of the MRCFM method and the accuracy of the co-simulation model are verified by experiments.

2. Sideband Component Feature Identification Based on DPWM

2.1. Principle of DPWM

The classical SVPWM follows the principle of vector proximity synthesis. Figure 1 shows the voltage space vector sector diagram of SVPWM. The six basic voltage vectors $U_1(100)$, $U_2(010)$, $U_3(110)$, $U_4(001)$, $U_5(101)$ and $U_6(011)$ together divide the plane into six sectors. The two zero vectors, $U_0(000)$ and $U_7(111)$, are located at the origin with an amplitude of zero and are only used to complement the vector action time. When the reference voltage vector U_{out} is located in a certain sector, its value can be synthesized by the two basic voltage vectors in the sector with the zero vector equivalent. Taking sector I

as an example, the reference voltage vector can be obtained according to the volt-second equilibrium principle as

$$\vec{U_{out}} = \vec{U_4}\frac{T_4}{T_S} + \vec{U_6}\frac{T_6}{T_S} + \vec{U_{0,7}}\frac{T_{0,7}}{T_S} \tag{1}$$

$$T_S = T_4 + T_6 + T_{0,7} \tag{2}$$

where T_S denotes the switching period. T_4, T_6 and $T_{0,7}$ denote the action times of the fundamental voltage vectors U_4, U_6 and the zero vector $U_{0,7}$, respectively.
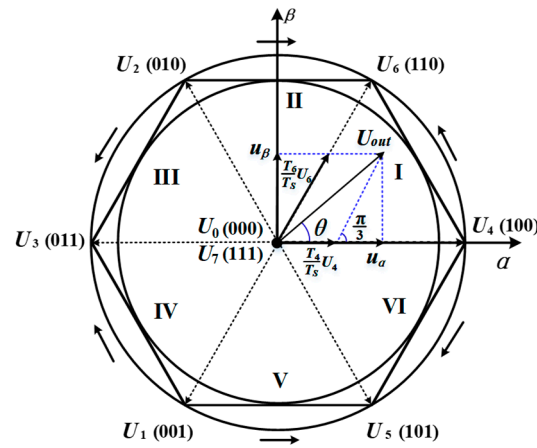

Figure 1. Diagram of the voltage space vector.

The most direct method of converting from CPWM to DPWM is to discard the zero vector. By selecting only a single zero vector in the whole switching cycle to compensate for the vector action time, the bridge arm of a phase of the inverter will be in the clamped state at a specific time. The switching sequence of DPWM is shown in Figure 2, which shows that due to the selection of only one zero vector, the switching sequence of the DPWM scheme becomes a five-segmented one. Different clamping methods can obtain six different DPWM modulation strategies, i.e., DPWMMIN, DPWMMAX, DPWM0, DPWM1, DPWM2 and DPWM3 [28].
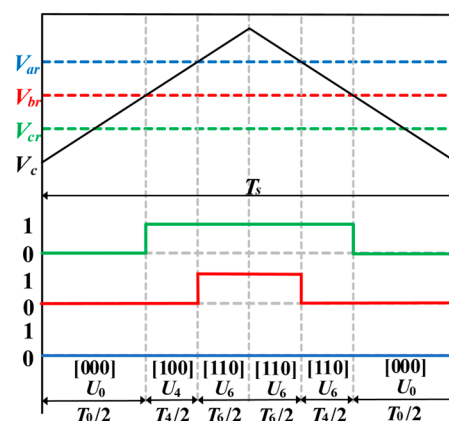

Figure 2. DPWM switching sequence in sector I.

2.2. Analysis of Sideband Current Harmonics and Radial Electromagnetic Force Characteristics

Sideband current harmonics can be investigated by constructing the double Fourier series in the frame of the stator coordinate system with the modulating wave frequency ω_0 and the carrier frequency ω_c as variable; the sideband harmonic components in the rotor coordinate system are then directly resolved by rearranging them through coordinate

transformations [6]. Taking the first carrier frequency domain as an example, when $n = 1$, ignoring the higher harmonics with smaller amplitudes, the sideband current harmonics in the DPWM can be shown as

$$
\begin{aligned}
i_h(t) \approx & \, \varepsilon_1 i_{\alpha_1} \cos[2\pi(\omega_c \pm \alpha_1\omega_0)t] + \\
& \, \varepsilon_2 i_{\alpha_2} \cos[2\pi(\omega_c \pm \alpha_2\omega_0)t] + \\
& \, \varepsilon_3 i_{\alpha_3} \cos[2\pi(\omega_c \pm \alpha_3\omega_0)t]
\end{aligned}
\tag{3}
$$

where $i_{\alpha 1}$, $i_{\alpha 2}$ and $i_{\alpha 3}$ denote the current harmonic amplitudes with eigenfrequencies $\omega_c \pm \alpha_1\omega_0$, $\omega_c \pm \alpha_2\omega_0$ and $\omega_c \pm \alpha_3\omega_0$, respectively. The specific values of α_1, α_2 and α_3 are shown in Table 1.

Table 1. The different DPWM modes correspond to ε_1, ε_2, ε_3, α_1, α_2, α_3.

DPWM Mode	ε_1	ε_2	ε_3	α_1	α_2	α_3
0	1	1	0	2	4	/
1	1	1	1	4	6	8
2	1	1	0	2	4	/
3	1	1	1	4	6	8
MAX	1	0	0	1	/	/
MIN	1	0	0	1	/	/

The amplitude of the sideband current harmonics depends on the modulation ratio and speed of the motor [29,30]. The distribution of current harmonics under different DPWM modes can be derived from Equation (3) and Table 1.

The vibro-acoustic response of PMSM is mainly caused by the electromagnetic force acting on the stator, and the radial electromagnetic force density can be defined by Maxwell's stress tensor method as

$$
f(\theta, t) = \frac{1}{2\mu_0}\left[B_r(\theta, t)^2 - B_t(\theta, t)^2\right] \approx \frac{1}{2\mu_0}B_r(\theta, t)^2
\tag{4}
$$

where B_r denotes the radial air-gap flux density. B_t denotes the tangential air-gap flux density. μ_0 denotes the vacuum permeability. Since B_r is much greater than B_t, the electromagnetic force effect generated by the tangential air-gap flux density is ignored.

Neglecting magnetic saturation effects and considering the principle of magnetic field superposition, as shown in Equation (5), the radial air-gap flux density B_r can be decomposed into the v-th stator armature magnetic field B_{arm_v} and the μ-th rotor permanent magnet magnetic field B_{mag_μ}.

$$
B_r(\theta, t) = B_{arm_v}(\theta, t) + B_{mag_u}(\theta, t)
\tag{5}
$$

$$
B_{arm\_v}(\theta, t) = \sum_{v=1}^{\infty} F_{arm\_v}\cos(vp\theta \pm \omega t) = \sum_{v=1}^{\infty} \frac{3\sqrt{2}NkI_{d/q}}{\pi vp}\cos(vp\theta \pm \omega t)
\tag{6}
$$

$$
B_{mag\_u}(\theta, t) = \sum_{\mu=1}^{\infty} F_{mag\_\mu}\cos(\mu p\theta \pm \omega t + \varphi) = \sum_{\mu=1}^{\infty} \frac{3\sqrt{2}NkI_{d/q}}{\pi\mu p}\cos(\mu p\theta \pm \omega t + \varphi)
\tag{7}
$$

where F_{arm_v} and F_{mag_μ} denote the stator armature electromotive force and permanent magnet electromotive force, respectively. N denotes the number of coil turns. p denotes the number of pole pairs. μ and v denote the harmonic orders of the permanent magnet magnetic field and the armature magnetic field, respectively. φ denotes the angle between the current vector and the α axis.

Given the relatively modest amplitude of both the fundamental armature field and the harmonic armature field, the calculation is simplified by only considering the sideband electromagnetic force that arises from the interaction between the permanent magnet field

and the harmonic armature field. By substituting Equations (5)–(7) into (4), the sideband radial electromagnetic force density can be presented as follows:

$$
\begin{aligned}
f_r(\theta,t) &\approx \frac{1}{2\mu_0}\left[\sum_{v=1}^{\infty}\frac{3\sqrt{2}NkI_{d/q}}{\pi vp}\cos(vp\theta\pm\omega t)+\sum_{\mu=1}^{\infty}\frac{3\sqrt{2}NkI_{d/q}}{\pi\mu p}\cos(\mu p\theta\pm\omega t+\varphi)\right]^2 \\
&\approx \frac{9N^2k^2}{\mu_0\pi^2 p^2}*\sum_{v}^{\infty}\sum_{h}^{\infty}\frac{I_{d/q}{}^2}{\mu v}\left\{\begin{array}{l}\cos\left[(p-vN_t)\theta-(\omega_0-\omega_c)t\right]+\\ \cos\left[(p+vN_t)\theta-(\omega_0+\omega_c)t\right]\end{array}\right\}
\end{aligned}
\tag{8}
$$

where N_t denotes the unit motor, numerically taking the maximum common factor of the motor pole pair number p and slot number z. k denotes the winding coefficient.

In Equation (8), it can be seen that the sideband electromagnetic force has obvious time-frequency characteristics. The frequency distribution of the major sideband harmonics can be expressed as $n\omega_c \pm k\omega_0$, where n and k are combinations of odd and even parities. Combining the sideband current harmonic characteristic frequencies near the first carrier frequency, when $n = 1$, the spatio-temporal characteristics of sideband components near the carrier frequency domain of the DPWM are shown in Table 2. Based on the above, the analytical model of the sideband harmonic components and radial electromagnetic force characteristics introduced by the conventional DPWM technique is completely established.

Table 2. Distribution of spatial and temporal characteristics of sideband components.

Current Harmonics	Magnetic Flux Density	Radial Electromagnetic Force
$\omega_c - 7\omega_0$	$\omega_c - 7\omega_0$	$\omega_c - 6\omega_0,\ \omega_c - 8\omega_0$
$\omega_c - 5\omega_0$	$\omega_c - 5\omega_0$	$\omega_c - 4\omega_0,\ \omega_c - 6\omega_0$
$\omega_c + 5\omega_0$	$\omega_c + 5\omega_0$	$\omega_c + 4\omega_0,\ \omega_c + 6\omega_0$
$\omega_c + 7\omega_0$	$\omega_c + 7\omega_0$	$\omega_c - 6\omega_0,\ \omega_c - 8\omega_0$

3. Principle and Implementation of Markov Chain Random Carrier Frequency Modulation

3.1. Principles of RCFM Technique and Random Number Analysis

Conventional PWM techniques employ fixed carrier frequency modulation, resulting in the sideband harmonic current spectrum concentrated in the carrier frequency and its multiples, which significantly affects the vibro-acoustics performance of the motor. By combining the carrier frequency with random numbers, the carrier frequency can be randomly varied within a certain range. The random carrier frequency ω_{n+1} after randomization of the original fixed carrier frequency ω_c can be expressed as

$$
\omega_{n+1} = \omega_c + R \cdot s
\tag{9}
$$

where s denotes the random number varying in the range of $(-1, 1)$. R denotes the random gain of the pseudo-random number generation strategy, which is specified in the spectrum as the spreading width of the sideband harmonic components.

The core of the RCFM technique is the random number generation strategy. The pseudo-random number generation method, linear congruential method, table look-up method and chaotic mapping method are usually used to generate random numbers. If the randomness of random numbers is good, the harmonic current will be uniformly distributed within the carrier frequency range, and the harmonic amplitude will be effectively reduced, thus further suppressing the vibration noise of the motor.

The modulation effect after the carrier frequency randomization is determined by the random value s and the random gain R at a certain moment, i.e., the carrier frequency varies within the range of $[\omega_c - R, \omega_c + R]$, and the PWM signal after asymmetric random modulation is shown in Figure 3. In addition, since RCFM does not impose restrictions on random number generation, it unavoidably results in random number values exceeding

or falling below the average expected value during the generation process. Consequently, the random carrier frequency affected by it will be larger or smaller than the center carrier frequency in a certain period of time, as shown in Figure 4.
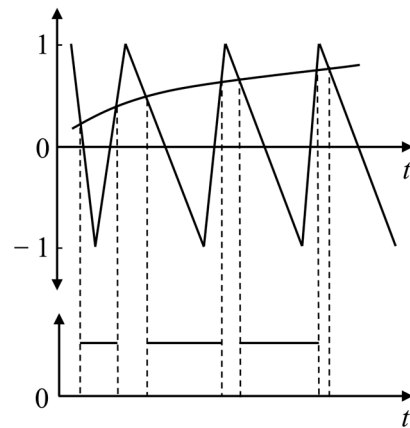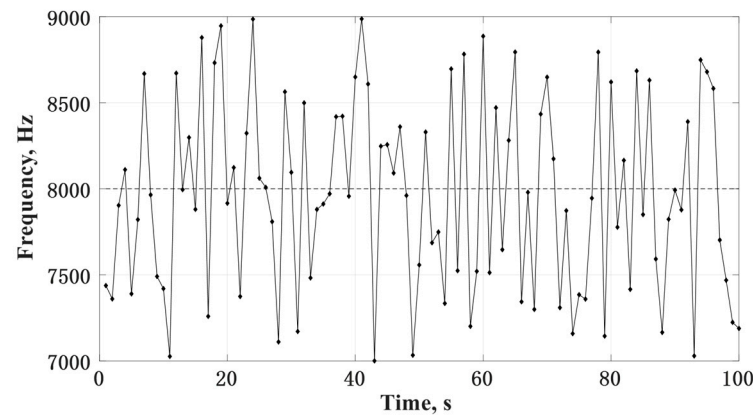

Figure 3. Schematic diagram of random PWM.

Figure 4. The simulation results of the carrier frequency in conventional RCFM.

3.2. Markov Chain Principle and Three-State Random Number Generation Process

For the traditional RCFM, there exists the problem of uneven distribution of random numbers in a short period of time, which results in increased pulsation components in phase current and switching losses. In this paper, a three-state Markov chain model is introduced to optimize the effect of random number generation, and the particle swarm optimization (PSO) algorithm is applied to select the optimal transition probabilities and random gains. The Markov process is known as a memoryless process, meaning that the value of the random event sequence at the next moment (a_{n+1}, t_{n+1}) is only related to the current value (a_n, t_n), which is independent of previous values, and the sequence of the continuity random numbers can be expressed as

$$M\{(a_{n+1}, t_{n+1})|(a_1, t_1), (a_2, t_2), \ldots, (a_n, t_n)\} = M\{(a_{n+1}, t_{n+1})|(a_n, t_n)\} \tag{10}$$

In the random optimization algorithm simulation and practical design, it is necessary to discretize the continuous events to form discrete Markov chains. Therefore, this paper introduces the conditional transition probability $P_{ij}(m,n)$ at a single moment, which can be denoted as

$$P_{ij}(m, n) = P\{X_n = a_j | X_m = a_i\} = P\{X_n = j | X_m = i\}, i, j \in S \tag{11}$$

where S denotes the state space, $S = \{a_1, a_2, \ldots, a_n\}$. The transition probability $P_{ij}(m,n)$ is the conditional probability that the system is in state a_i at time m and transitions to state a_j after $(n - m)$ time steps; it can also be interpreted as the probability that the system transitions from state i at time m to state j at time n.

The random number generation module only needs to consider the value of the previous moment, and it only takes one step from time m to time n. This type of Markov chain is called a homogeneous Markov chain with stationary transition probabilities. $P_{ij}(m,m + 1)$ is denoted as $P_{ij}(m)$, i.e.,

$$P_{ij}(m) = P_{ij} = P\{X_{m+1} = j | X_m = i\}, i, j \in S \tag{12}$$

Representing all transition probabilities in the above homogeneous Markov chain in the matrix form, the transition probability matrix P is

$$P = \{p_{ij}, i, j \in S\} = \begin{bmatrix} p_{11} & \cdots & p_{1m} \\ \vdots & \ddots & \vdots \\ p_{n1} & \cdots & p_{nm} \end{bmatrix} \tag{13}$$

where each element of P belongs to the value of [0,1], and the sum of the elements in each row and column is 1.

Based on the above, it can be seen that the larger the state space, the more elements the transition matrix contains, which also means that the effect of optimized random numbers is more ideal. However, the increase in random state space will also bring additional computation to the chip processor. Considering the effect of optimized random numbers and the amount of computation, this paper chooses to introduce the three-state Markov chain into the RCFM technique.

The design of three-state Markov chain random carrier frequency modulation is to divide the original carrier frequency variation interval $[\omega_c - R, \omega_c + R]$ into three parts: $[\omega_c - R, \omega_c - k \times R]$, $[\omega_c - k \times R, \omega_c + k \times R]$ and $[\omega_c + k \times R, \omega_c + R]$, with k denoting the modulation coefficient and $k \in (0, 0.33)$. The three parts correspond to states 1, 2 and 3, respectively. The state of the next carrier frequency is determined by the judgment of the state of the current carrier frequency. Figure 5 shows the state parameter transition diagram of three-state Markov chain carrier frequency.
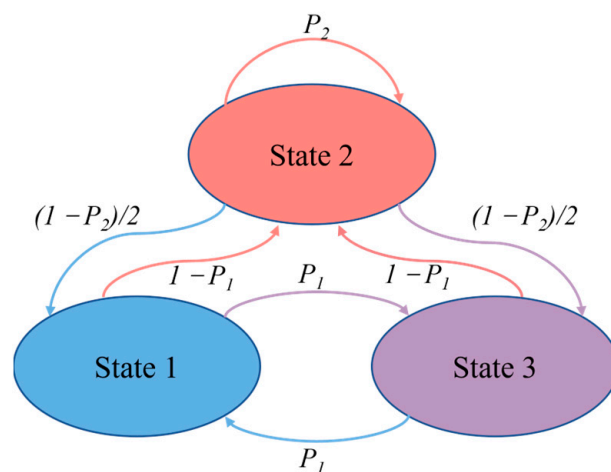
Figure 5. State parameter transition diagram of three-state Markov chain carrier frequency.

In Figure 5, it can be seen that if the current carrier frequency of the system belongs to state 1, the next generated carrier frequency of the system can only belong to state 2 or 3, and the probability of belonging to state 3 is P_1, while the probability of belonging to state 2 is $1 - P_1$. If the current carrier frequency of the system belongs

to state 2, then the probability of the next generated carrier frequency still belonging to state 2 is P_2, while the probabilities of being in state 1 or 3 are both $(1 - P_2)/2$. If the current carrier frequency of the system belongs to state 3, the next generated carrier frequency of the system can only belong to state 1 or 2, where the probability of being in state 1 is P_1, and the probability of being in state 2 is $1 - P_1$. If the current carrier frequency of the system belongs to state 3, the next generated carrier frequency of the system can only belong to state 1 or 2, where the probability of belonging to state 1 is P_1, and the probability of belonging to state 2 is $1 - P_1$. Therefore, the transition probability matrix of the three-state Markov chain can be expressed as

$$
P = \begin{bmatrix} p_{11} & p_{12} & p_{13} \\ p_{21} & p_{22} & p_{23} \\ p_{31} & p_{32} & p_{33} \end{bmatrix} = \begin{bmatrix} 0 & p_1 & 1 - p_1 \\ (1 - p_1)/2 & p_2 & (1 - p_1)/2 \\ 1 - p_1 & p_1 & 0 \end{bmatrix} \tag{14}
$$

where p_1 and p_2 take the values of $(0, 1)$.

The three-state Markov chain random carrier frequency generation result is shown in Figure 6. Compared with the conventional random carrier frequency generation results, the performance of random numbers is further improved, and the randomized carrier frequency distribution is more uniform, which verifies the effectiveness of the three-state Markov chain random number algorithm.
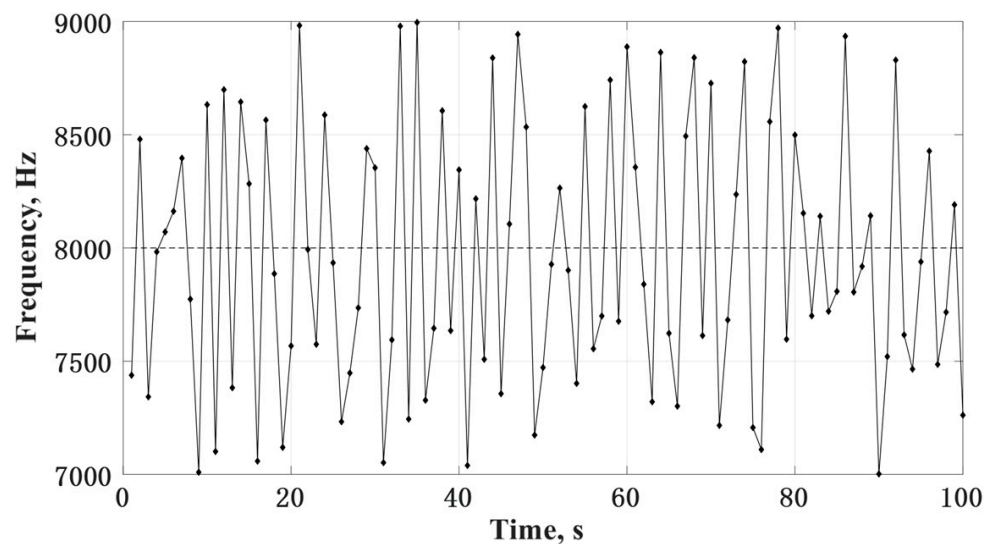

Figure 6. The random carrier frequency results with three-state Markov chain.

3.3. Random Parameter Optimization Based on Particle Swarm Optimization Algorithm

Based on the above analysis, it can be seen that the random gain R and the transition probability P have significant effects on the modulation effect after the carrier frequency randomization, and these two parameters need to be constrained to the range of values in the design of the system parameters. In order to improve the computational speed, particle swarm optimization (PSO) algorithm is chosen to quickly find the optimal R and P parameters. Based on the optimal random parameters, three-state Markov chain random carrier frequency modulation is introduced to improve the random carrier frequency distribution, so as to meet the optimal sideband harmonic components and vibro-acoustic response suppression effects.

As a stochastic search algorithm, the core driving factor of the PSO algorithm is to share and update the global historical optimal solution G_{best} with the individual historical optimal solution P_{best}, so as to realize the optimal solution of the individual extremum and the particle swarm globally, and the specific process is shown in Figure 7.
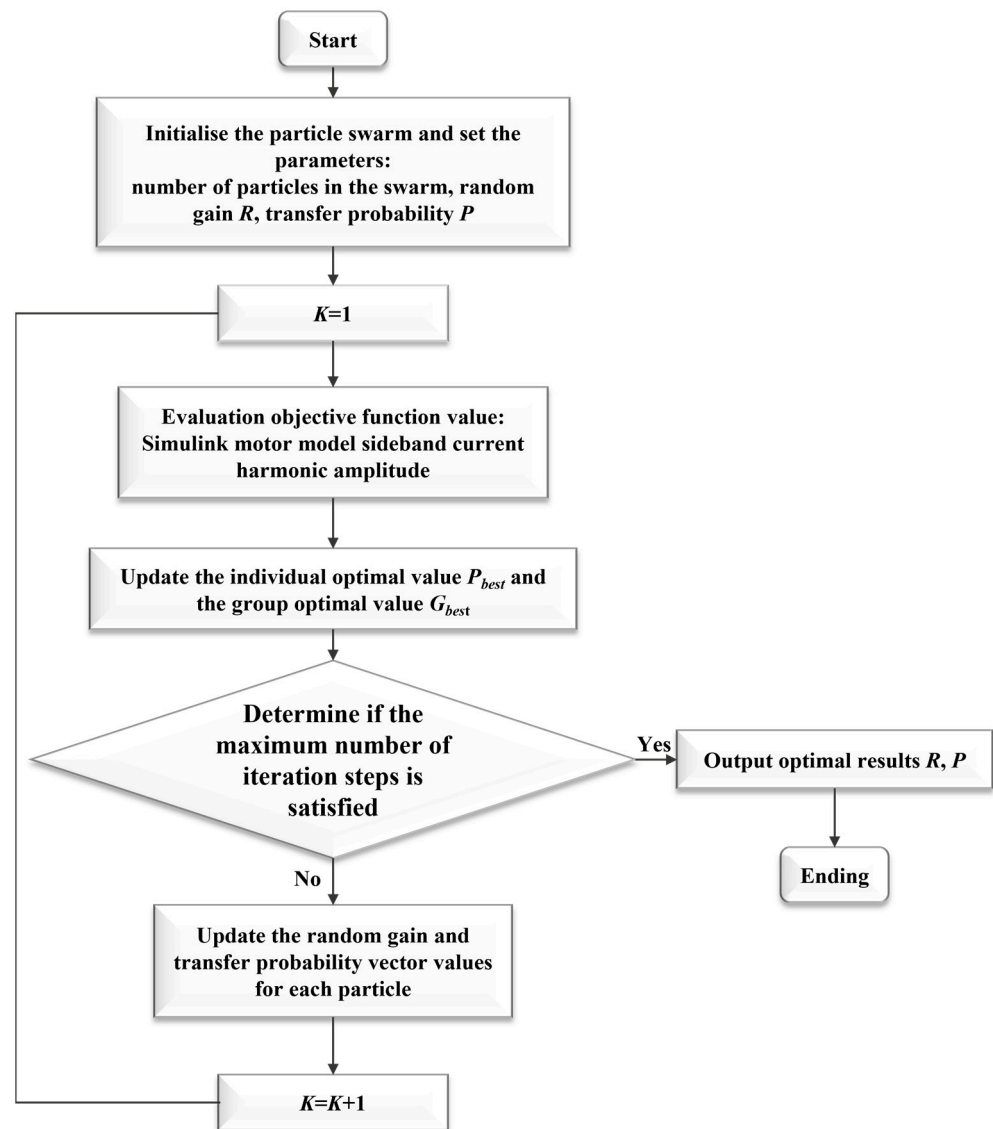
Figure 7. Flowchart of particle swarm optimization.

The results of the random parameter optimization based on the PSO algorithm are shown in Figure 8. During the iteration process, the maximum number of iterative steps is set to 60, and the error value of the objective function stabilizes within 40 iterative steps, indicating that the suppression effect of sideband current harmonics reaches the optimization. At this time, the value of the transition probability P is 0.68. Figure 8b shows that the peak value of sideband harmonics decreases with the increase in stochastic gain R and reaches the optimal effect at $R = 2000$. Figure 8c shows that the suppression of sideband harmonics response tends to be saturated when the value of R is larger than 2000 Hz. According to the above random parameter optimization analysis, setting the transition probability P to 0.68 and the random gain R to 2000 can optimize the suppression effect of sideband current harmonics.
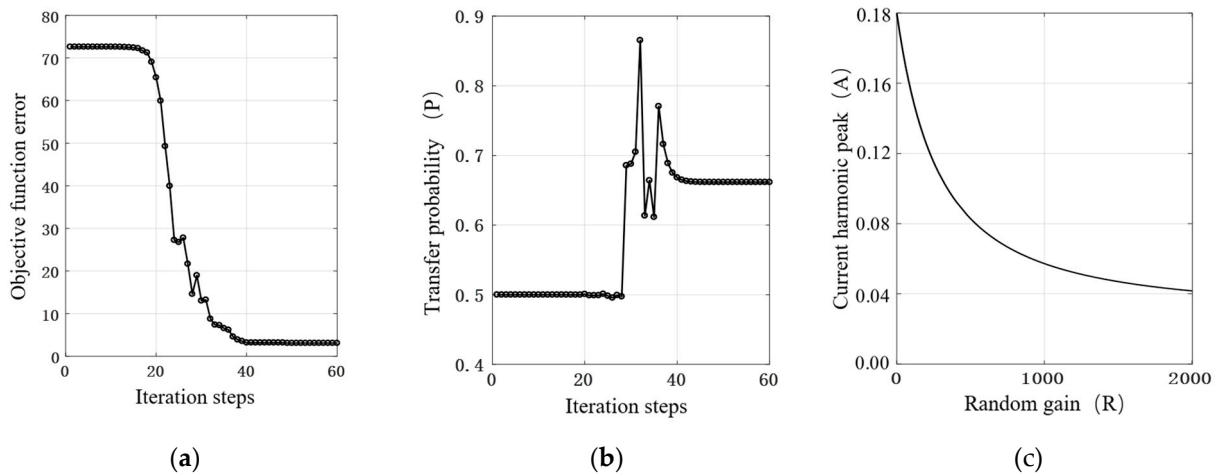
Figure 8. Results of randomized parameters with PSO algorithm: (**a**) The error of the objective function; (**b**) The value of the transfer probability; (**c**) The value of the random gain.

## 4. Analytical Prediction of the Suppressive Impact of MRCFM on Sideband Constituents

4.1. Analysis and Prediction of Sideband Current Harmonic Suppression Effect

In this paper, a vector control model of PMSM is established in JMAG via field-circuit coupling. Table 3 displays the main parameters of the motor. Considering that the operational range of the test prototype is 500~1500 r/min and 2~6 Nm, 1000 r/min and 4 Nm are therefore chosen as the steady running conditions to simulate and analyze the harmonic currents before and after the adoption of the MRCFM method.

Table 3. Key parameters of the prototype.

Parameters	Values	Parameters	Values
Number of slots	12	Rated torque	8 Nm
Number of poles	10	d-axis inductance	1.2 mH
Rated speed	2000 r/min	q-axis inductance	3.4 mH
Rated power	3 kW	DC link voltage	300 V

The second carrier frequency domain is beyond the range of the sensitive frequency band of the human ear; therefore, the simulation prediction and verification in this paper only focus on the sideband components near the first carrier frequency domain. Figure 9 displays the simulated frequency spectra of the sideband harmonics in the phase current for six pulse-width modulation techniques, using ω_c = 8 kHz and ω_0 = 83.33 Hz as the carrier frequency. The characteristic frequencies corresponding to the main-order components of DPWMMIN and DPWMMAX are $\omega_c \pm \omega_0$. The sideband current harmonic distributions of DPWM0 and DPWM2 are located in $\omega_c \pm 2\omega_0$ and $\omega_c \pm 4\omega_0$. The main-order components of DPWM1 and DPWM3 are extended to farther bands, located at $\omega_c \pm 3\omega_0$, $\omega_c \pm 5\omega_0$ and $\omega_c \pm 7\omega_0$. As shown in Figure 10, after adopting the MRCFM method, the peak values of sideband current harmonics for various PWM strategies decrease significantly. The harmonic peak values of DPWMMIN/MAX, DPWM0/2 and DPWM1/3 decrease by 33.0%, 33.3% and 38.5%, respectively.
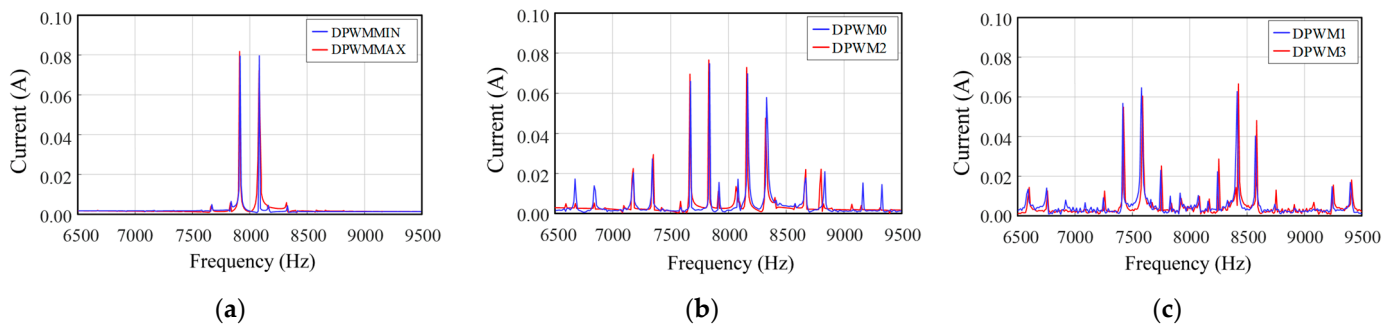
Figure 9. Simulation prediction of sideband current harmonics under different PWM strategies: (**a**) DPWMMIN and DPWMMAX; (**b**) DPWM0 and DPWM2; (**c**) DPWM1 and DPWM3.
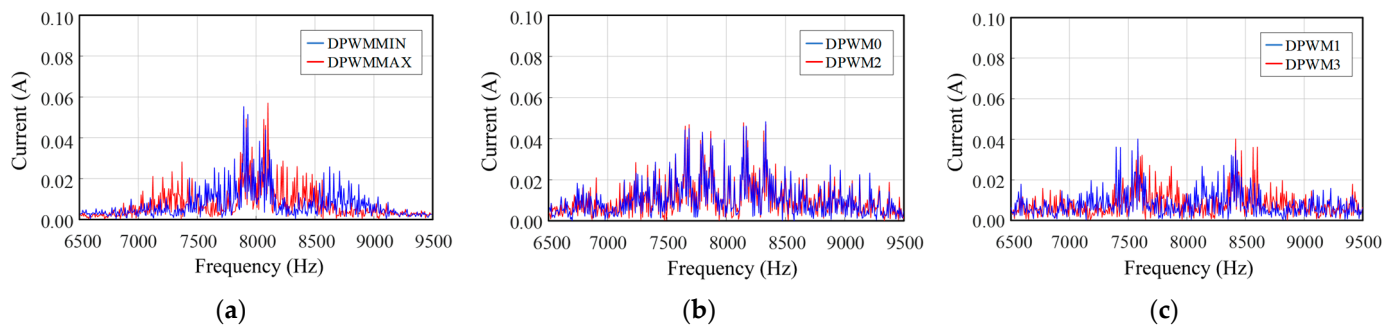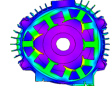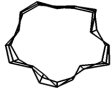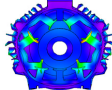

Figure 10. Prediction of the suppression effect of Markov chain random carrier frequency modulation on sideband current harmonics of different PWM strategies: (**a**) DPWMMIN and DPWMMAX; (**b**) DPWM0 and DPWM2; (**c**) DPWM1 and DPWM3.

4.2. Modal Analysis

The structural characteristics of the motor have a large impact on its vibration noise. Resonance occurs when the frequency of electromagnetic force closely matches the natural frequency, which in turn worsens the NVH performance of the motor [31]. In this paper, finite element analysis is performed in JMAG to obtain the modal parameters of the prototype. Since the electromagnetic force is almost uniformly distributed along the axial direction, the circumferential mode contributes the most to the vibration. To validate the precision of the finite element model, the modal experiments are carried out in this paper using the moving force hammer method. During the experiment, the prototype is suspended by an elastic rope, and five acceleration sensors are placed to obtain the vibration response of the shell surface. The measured and simulated modal shapes and frequencies are shown in Table 4, and the front cover is hidden in the simulation results to visualize the vibration shapes of each order. The results show that the relative errors between measurement and simulation are within 5%, which indicates the accuracy of the finite element model.

**Table 4.** Experimental validation of modal parameters.

Modal Order	Measured Result	Simulation Result	Relative Error
2	1396.5 Hz	1437.4 Hz	2.9%
3	2047.1 HZ	2055.3 Hz	0.4%
4	2891.2 Hz	2861.5 Hz	1.0%
5	3645.7 Hz	3475.6 Hz	4.6%

4.3. Analysis and Prediction of Sideband Vibration Suppression Effects

To forecast the suppressive effect of MRCFM on vibro-acoustics, this paper develops a Simulink and JMAG multi-physics field co-simulation model. The calculation process is shown in Figure 11. Firstly, the electromagnetic force on the inner surface of the stator tooth is calculated by the two-dimensional electromagnetic model of the motor, and the nodal force is mapped into the structural model as an excitation. Finally, the vibration response of the prototype is calculated by the modal superposition method [32]. The equation of the modal superposition method can be expressed as

$$\{F\} = [M]\sum_{i}^{N}\{\Phi_i\}\ddot{y}_i + [C]\sum_{i}^{N}\{\Phi_i\}\dot{y}_i + [K]\sum_{i}^{N}\{\Phi_i\}y_i \tag{15}$$

where $[M]$, $[C]$ and $[K]$ denote the mass, damping and stiffness matrices, respectively. N denotes the superimposed modal order. Φ_i denotes the *i*-th order modal vibration mode. y_i denotes the displacement in the modal coordinate system of the node.
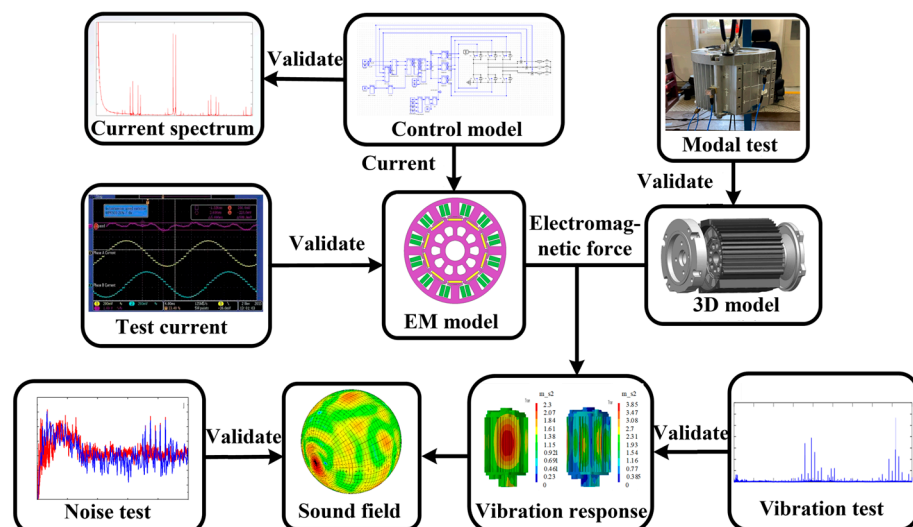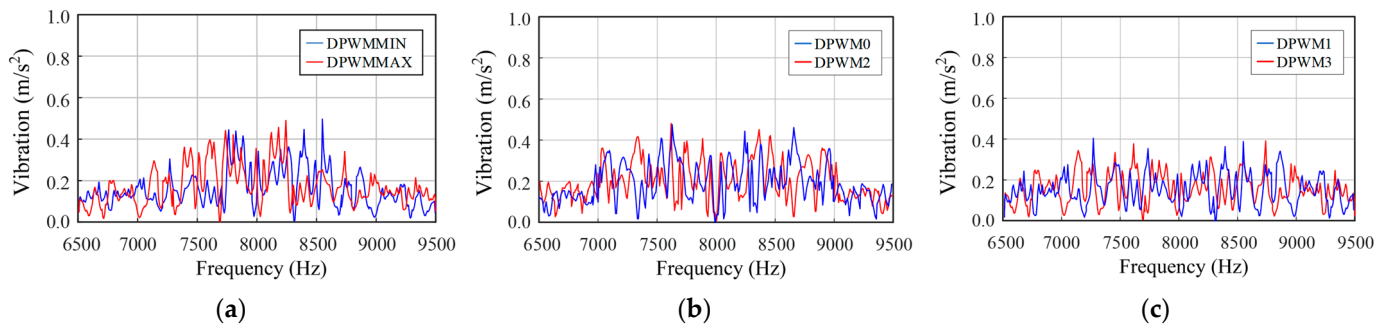

Figure 11. The multi-physics field analysis process for electromagnetic noise of PMSM.

The sideband vibration response spectra of the prototype with different PWM strategies are shown in Figure 12, which shows that the unoptimized PWM strategies have obvious order characteristics. Figure 13 shows the sideband vibration response spectra of the PWM strategies after the introduction of the MRCFM method. After the introduction of the MRCFM method, the PWM strategies no longer have significant main-order components, and the sideband vibration response amplitude is smaller and uniformly distributed. The peak sideband vibration responses are reduced by 36.7%, 39.5% and 42.0% for DPWMMIN/MAX, DPWM0/2 and DPWM1/3, respectively.
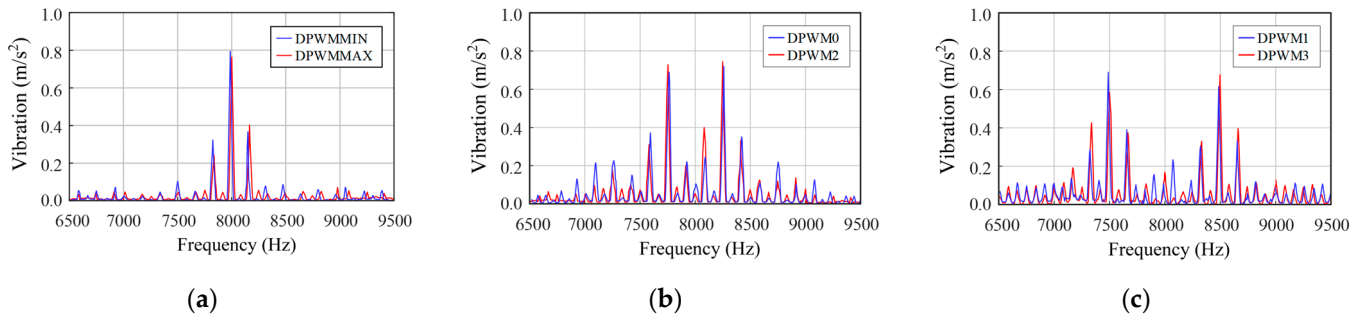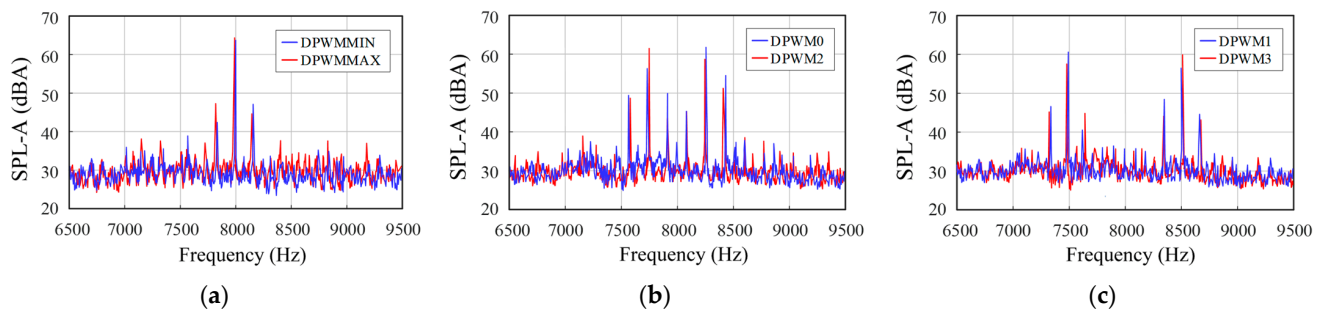

Figure 12. Simulation prediction of sideband vibration response under different PWM strategies: (**a**) DPWMMIN and DPWMMAX; (**b**) DPWM0 and DPWM2; (**c**) DPWM1 and DPWM3.
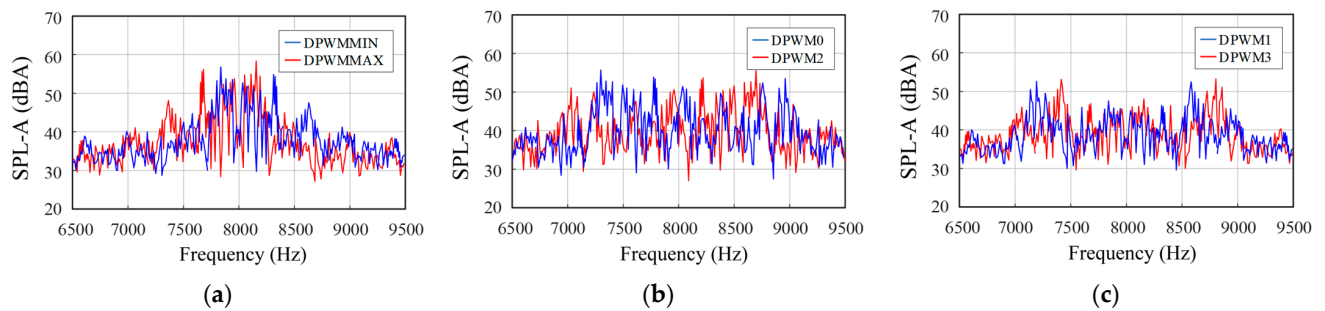

Figure 13. Prediction of the suppression effect of Markov chain random carrier frequency modulation on sideband vibration response of different PWM strategies: (**a**) DPWMMIN and DPWMMAX; (**b**) DPWM0 and DPWM2; (**c**) DPWM1 and DPWM3.

4.4. Analysis and Prediction of Sideband Acoustic Suppression Effects

In order to investigate the sideband acoustic responses caused by different PWM strategies, simulation analysis is conducted using the multi-physics field simulation model mentioned above, and the obtained acoustic results are processed by using the A-weighting of the sound pressure level (SPL-A). The sideband acoustic response spectra of the prototype with different PWM strategies are shown in Figure 14. Combined with the vibration results, it can be seen that the sideband electromagnetic noise caused by PWM strategies has peak features corresponding to the vibration response. Figure 15 shows the sideband acoustic response spectra of each PWM strategy after the introduction of the MRCFM method. The peaks of the sideband acoustic responses of each strategy are significantly reduced; DPWMMIN/MAX, DPWMMIN/MAX, DPWM0/2 and DPWM1/3 are reduced by 15.3%, 12.9% and 12.7%, respectively, corresponding to optimization amplitudes of 7~9 dBA.

Figure 14. Simulation prediction of sideband acoustic response under different PWM strategies: (**a**) DPWMMIN and DPWMMAX; (**b**) DPWM0 and DPWM2; (**c**) DPWM1 and DPWM3.

Figure 15. Prediction of the suppression effect of Markov chain random carrier frequency modulation on sideband acoustic response of different PWM strategies: (**a**) DPWMMIN and DPWMMAX; (**b**) DPWM0 and DPWM2; (**c**) DPWM1 and DPWM3.

5. The Validation of Experiments

5.1. Experiment Platform for the Test

In order to verify the effectiveness of MRCFM and the accuracy of the multi-physics field numerical prediction model, this paper conducts vibration and noise response tests using various PWM strategies mentioned in the paper. For comparison and verification with the simulation results, the experiments are still chosen to be conducted at 1000 r/min and 4 Nm working conditions, and other parameter settings are consistent with the simulation predictions from the previous paper. The experimental platform is positioned in a semi-anechoic chamber environment to minimize the impact of background noise. Figure 16 shows the layout of the PMSM vibration noise test system. Based on the dSPACE semi-physical simulation platform, MATLAB/Simulink and the motor controller are used to achieve the hardware-in-the-loop real-time control. The phase current signals are recorded by the Teletronix-A622 current probe. The torque-speed power sensor of TSP type is used for the measurement of torque speed. The ICP-type three-channel accelerometer, microphone and the front-end of the LMS are used to acquire the acoustic vibration signals and subsequently analyzed using the accompanying software LMS Test.Lab 2021.1.
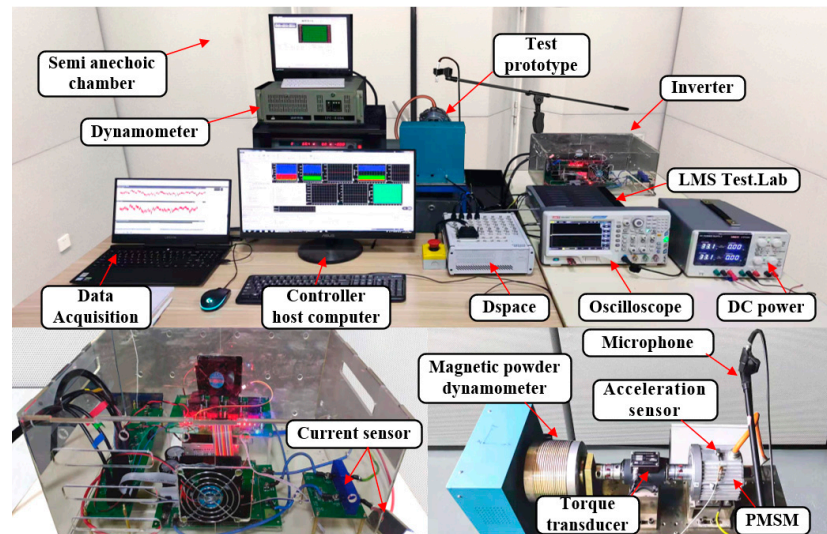
Figure 16. The PMSM vibration noise test system.

5.2. The Sideband Current Harmonics Comparative Test

In order to validate the precision of the simulation prediction results, the sideband current harmonic spectra of the prototype under steady state operating conditions are verified and analyzed. Figure 17 shows the phase current sideband harmonic spectra of six classical generalized DPWMs before and after MRCFM optimization. It can be seen that DPWMs with fixed carrier frequency modulation have obvious main-order components whose distribution characteristics are basically consistent with the simulation prediction results mentioned above. The peak values of the sideband current harmonics of the optimized DPWMs are significantly reduced. The harmonic components originally concentrated near the carrier frequency are uniformly spread to its surroundings, which shows that the MRCFM has a good harmonic suppression effect. Figure 18 shows the comparison curves between the simulated and measured peak values of the sideband current harmonics of different PWM strategies. It can be seen that the simulated and measured results are very close to each other with an error of no more than 0.004 A, which verifies the accuracy of the numerical prediction model of multi-physics field.
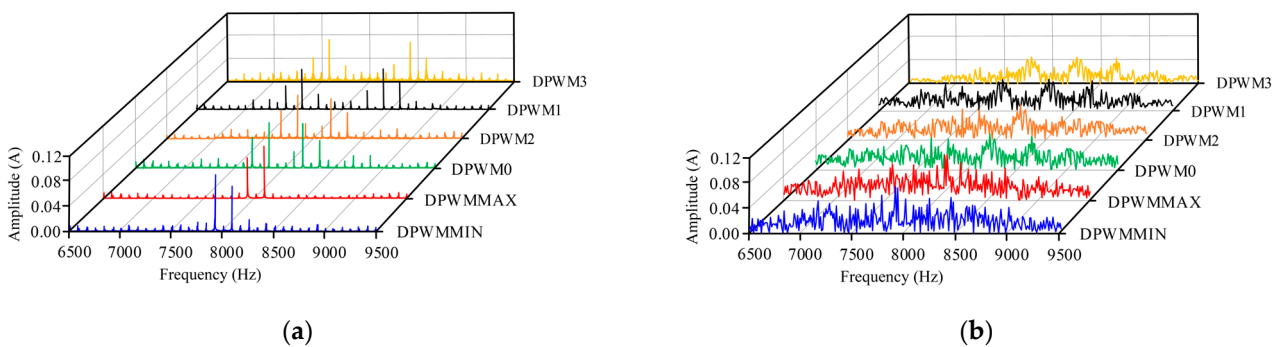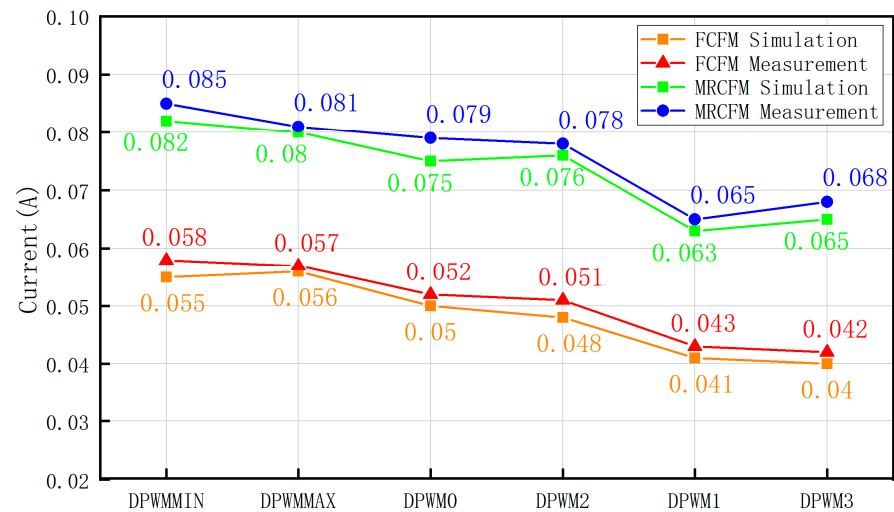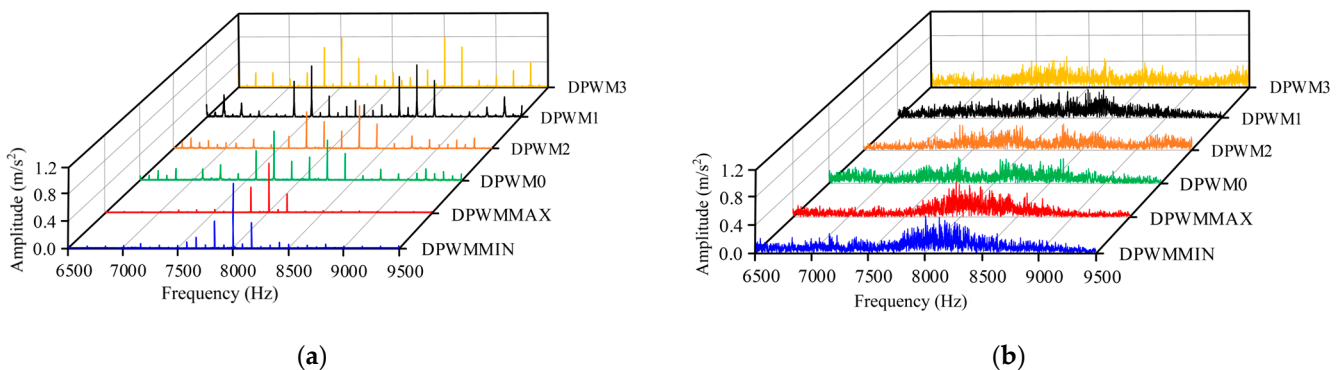

Figure 17. Experimental comparison of sideband current harmonics before and after MRCFM optimization: (**a**) Fixed carrier frequency modulation; (**b**) Markov chain random carrier frequency modulation.

Figure 18. Comparison of simulated and measured harmonic peaks of sideband currents with different modulation strategies.
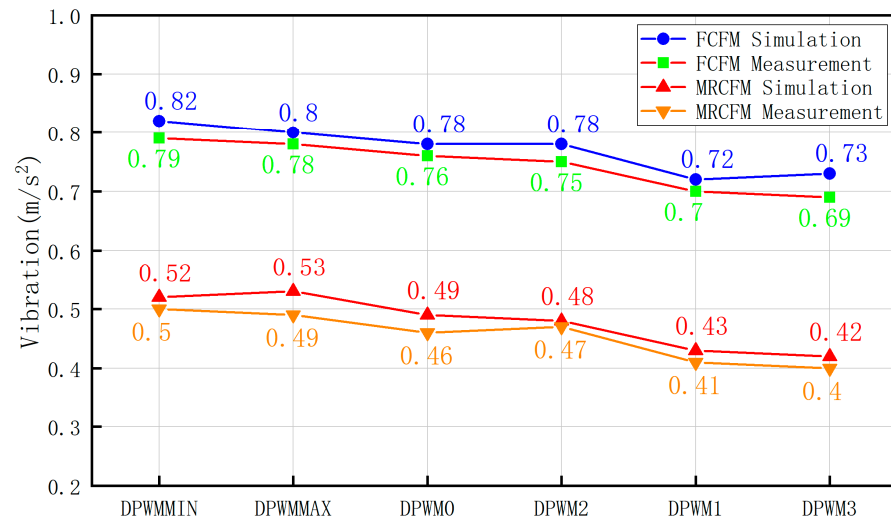
5.3. The Sideband Vibration Comparative Test

To confirm that the MRCFM approach can effectively suppress the sideband vibration response, vibration response tests are conducted on the experimental prototypes under various PWM modulation strategies. Figure 19 shows the measured sideband vibration response spectra of six classical generalized DPWMs before and after MRCFM optimization. It can be seen that the vibration response of DPWMs without optimization is mainly concentrated near the carrier frequency and corresponds to the distribution characteristics of current harmonics, further confirming that the sideband current harmonics are the main factors causing high-frequency vibration of PMSM. Combining the analysis results of the previous simulation prediction section, it can be seen that the multi-physical coupled numerical prediction model can accurately predict the characteristics of sideband vibration response of the prototype. The main-order components of various PWM strategies disappear, and the vibration peaks decrease significantly after optimization. Figure 20 displays the comparison curve of simulated and measured peak values of sideband vibration response of the prototype using different PWM strategies. It can be seen that MRCFM has a significant suppression effect on sideband vibration response caused by PWM strategies. The simulated values are slightly lower than the measured values, but the vibration error is not exceeding 0.04 m/s^2.

(a)

(b)

Figure 19. Experimental comparison of sideband vibration response before and after MRCFM optimization: (**a**) Fixed carrier frequency modulation; (**b**) Markov chain random carrier frequency modulation.
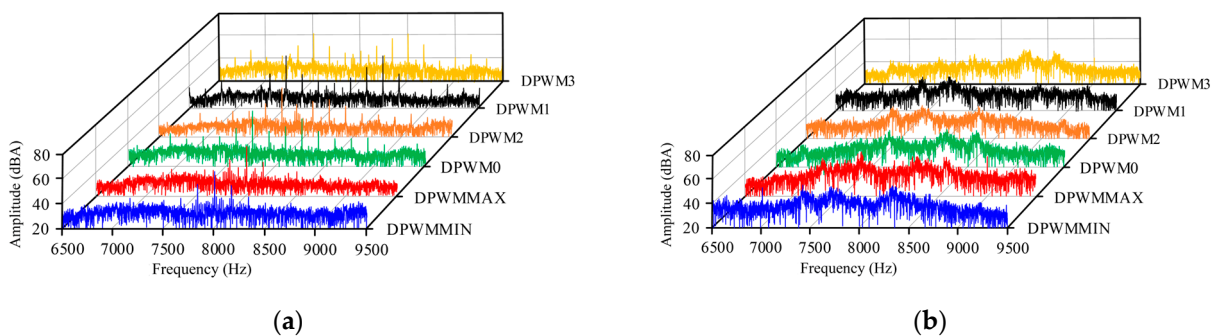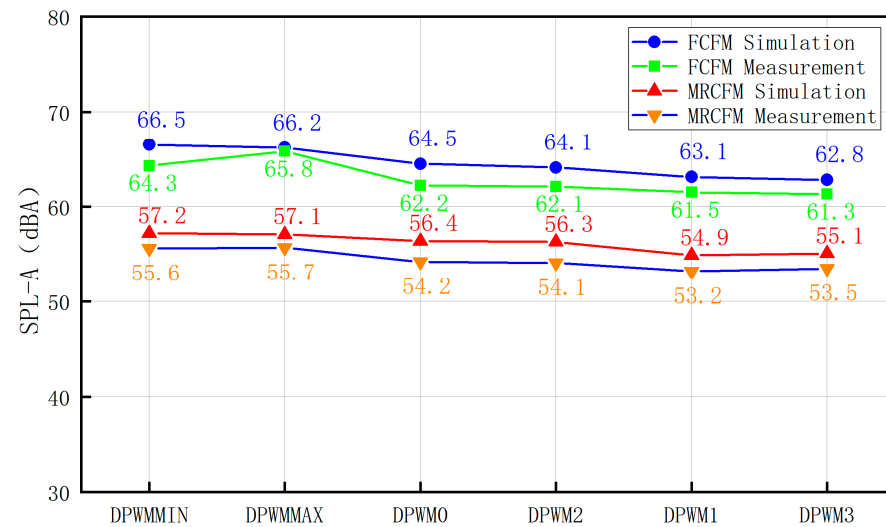
Figure 20. Comparison of simulated and measured peak sideband vibration response with different modulation strategies.

5.4. The Sideband Acoustic Comparative Test

To confirm that MRCFM can suppress the sideband acoustic response of PWM strategies, this paper conducts noise tests on the prototypes under different PWM strategies. In order to better reflect the real experience of the human ear in the measured noise, the acoustic data obtained from the experimental acquisition are subjected to A-weighting of the sound pressure level (SPL-A). Figure 21 presents the sideband acoustic response spectra of different PWM strategies. The primary characteristics of the DPWM acoustic response resemble the vibration signal. The sideband noise peaks caused by various PWM strategies are all over 61.0 dBA without optimization. After the optimization of MRCFM, the acoustic response spectra of various PWM strategies are uniformly distributed, and the peaks of the sideband noises are all less than 57.2 dBA. Figure 22 shows the comparison curves between simulated and measured sideband acoustic response peaks of various PWM strategies. The simulation results are fundamentally consistent with the measured results, which verifies the accuracy of the theoretical analysis and the multi-physics numerical prediction model. After optimization, each PWM's peak sideband acoustic response drops by 7–9 dBA. The results reveal that the MRCFM has a better suppression effect on the sideband acoustic response generated by the PWM strategy.

Figure 21. Experimental comparison of sideband acoustic response before and after MRCFM optimization: (**a**) Fixed carrier frequency modulation; (**b**) Markov chain random carrier frequency modulation.

Figure 22. Comparison of simulated and measured peak sideband acoustic response for different modulation strategies.

6. Conclusions

This paper proposes a MRCFM approach to suppress the DPWM-induced sideband harmonic and vibro-acoustic components. The multi-physical field co-simulation prediction model is developed to numerically forecast the spectral distribution and amplitude characteristics of the sideband vibro-acoustic response with different PWM strategies. According to the research results, the conclusions are as follows:

(1) The proposed MRCFM can effectively optimize the performance of random numbers, further optimizing the sideband current harmonics and vibro-acoustic response, and the distribution of the sideband spectrum shows better uniformity. The optimal noise suppression effect can reach 11 dBA.

(2) The co-simulation model constructed based on multi-physics fields can accurately predict the sideband vibro-acoustic response of each DPWM scheme. The error between the simulation results and the measured results is within 8%, which verifies the accuracy of the co-simulation prediction model with multi-physics fields.

(3) The proposed PSO optimization algorithm can effectively optimize the random gain *R* and the transition probability *P*, and the analysis method proposed in this paper can be applied to the prediction and analysis of sideband acoustic vibration of PMSM under various PWM strategies, which can provide a new idea for the identification and optimization of sideband acoustic vibration characteristics of PMSM.

Institutional Review Board Statement: Not applicable.

Informed Consent Statement: Not applicable.

Data Availability Statement: The data presented in this study are available on request from the corresponding author.

Conflicts of Interest: Author Liming Zhang was employed by the company Wuhan Fareo Automotive Parts Co., Ltd. Author Kefu Yao was employed by the company Dongfeng Liuzhou motor Co., Ltd. The remaining authors declare that the research was conducted in the absence of any commercial or financial relationships that could be construed as a potential conflict of interest.

Abbreviations

Abbreviations

MRCFM	Markov chain random carrier frequency modulation	PMSM	Permanent magnet synchronous motor
DPWM	Discontinuous pulse-width modulation	VSI	Voltage source inverter
RCFM	Random carrier frequency modulation	PWM	Pulse-width modulation
NVH	Noise, vibration and harshness	PSO	Particle swarm optimization
CPWM	Continuous pulse-width modulation	SVPWM	Space vector pulse-width modulation

Nomenclature

T_S	Switching period	ω_0	Modulating wave frequency
ω_c	Carrier frequency	$i_{\alpha 1}, i_{\alpha 2}, i_{\alpha 3}$	Current harmonic amplitude
B_r	Radial air-gap flux density	B_t	Tangential air-gap flux density
μ_0	Vacuum permeability	B_{arm}	Stator armature magnetic field
B_{mag}	Rotor permanent magnet magnetic field	F_{mag}	Permanent magnet electromotive force
F_{arm}	Stator armature electromotive force	N	Number of coil turns
p	Number of pole pairs	N_t	Unit motor
μ, v	Harmonic orders	k	Winding coefficient
$[M]$	Mass matrix	$[C]$	Damping matrix
$[K]$	Stiffness matrix	N	Modal order

References

1. Lin, F.; Zuo, S.; Deng, W.; Wu, S. Noise Prediction and Sound Quality Analysis of Variable-Speed Permanent Magnet Synchronous Motor. *IEEE Trans. Energy Convers.* **2017**, *32*, 698–706. [CrossRef]
2. Yang, Z.; Shang, F.; Brown, I.P.; Krishnamurthy, M. Comparative Study of Interior Permanent Magnet, Induction, and Switched Reluctance Motor Drives for EV and HEV Applications. *IEEE Trans. Transp. Electrif.* **2015**, *1*, 245–254. [CrossRef]
3. Huang, Y.; Xu, Y.; Li, Y.; Yang, G.; Zou, J. PWM Frequency Voltage Noise Cancelation in Three-Phase VSI Using the Novel SVPWM Strategy. *IEEE Trans. Power Electron.* **2018**, *33*, 8596–8606. [CrossRef]
4. Hu, S.; Zuo, S.; Liu, M.; Wu, H.; Liu, Z. Modeling and Analysis of Radial Electromagnetic Force and Vibroacoustic Behaviour in Switched Reluctance Motors. *Mech. Syst. Signal Process.* **2020**, *142*, 106778. [CrossRef]
5. Xu, Y.; Yuan, Q.; Zou, J.; Li, Y. Analysis of Triangular Periodic Carrier Frequency Modulation on Reducing Electromagnetic Noise of Permanent Magnet Synchronous Motor. *IEEE Trans. Magn.* **2012**, *48*, 4424–4427. [CrossRef]
6. Liang, W.; Wang, J.; Luk, P.C.-K.; Fang, W.; Fei, W. Analytical Modeling of Current Harmonic Components in PMSM Drive with Voltage-Source Inverter by SVPWM Technique. *IEEE Trans. Energy Convers.* **2014**, *29*, 673–680. [CrossRef]
7. Zhang, W.; Xiao, L.; Xu, Y.; Zou, J. PWM Harmonics Reduction for Dual-Branch Three-Phase PMSMs Using Interleaving Topology. *Energy Rep.* **2023**, *9*, 190–194. [CrossRef]
8. Liu, J.-K.; Yao, X.-D.; Liu, H.-L. PWM Harmonic Cancellation of Permanent Magnet Synchronous Motor Based on Periodic Spread Spectrum Modulation. *J. Electr. Eng. Technol.* **2024**, *19*, 2413–2423. [CrossRef]
9. Fang, Y.; Zhang, T. Sound Quality of the Acoustic Noise Radiated by PWM-Fed Electric Powertrain. *IEEE Trans. Ind. Electron.* **2018**, *65*, 4534–4541. [CrossRef]
10. Wang, L.; Wang, X.; Li, N.; Li, T. Modelling and Analysis of Electromagnetic Force, Vibration, and Noise in Permanent Magnet Synchronous Motor for Electric Vehicles under Different Working Conditions Considering Current Harmonics. *IET Electr. Power Appl.* **2023**, *17*, 952–964. [CrossRef]
11. Cassat, A.; Espanet, C.; Coleman, R.; Burdet, L.; Leleu, E.; Torregrossa, D.; M'Boua, J.; Miraoui, A. A Practical Solution to Mitigate Vibrations in Industrial PM Motors Having Concentric Windings. *IEEE Trans. Ind. Appl.* **2012**, *48*, 1526–1538. [CrossRef]
12. Tsoumas, I.P.; Tischmacher, H. Influence of the Inverter's Modulation Technique on the Audible Noise of Electric Motors. *IEEE Trans. Ind. Appl.* **2014**, *50*, 269–278. [CrossRef]
13. Schulz, S.E.; Kowalewski, D.L. Implementation of Variable-Delay Random PWM for Automotive Applications. *IEEE Trans. Veh. Technol.* **2007**, *56*, 1427–1433. [CrossRef]
14. Zhang, W.; Xu, Y.; Huang, H.; Zou, J. Vibration Reduction for Dual-Branch Three-Phase Permanent Magnet Synchronous Motor with Carrier Phase-Shift Technique. *IEEE Trans. Power Electron.* **2020**, *35*, 607–618. [CrossRef]
15. Xu, Y.; Yuan, Q.; Zou, J.; Yao, Y.; Zhu, G. Sinusoidal Periodic Carrier Frequency Modulation in Reducing Electromagnetic Noise of Permanent Magnet Synchronous Motor. *IET Electr. Power Appl.* **2013**, *7*, 223–230. [CrossRef]
16. Qiu, Z.; Chen, Y.; Liu, X.; Kang, Y.; Liu, H. Analysis of the Sideband Current Harmonics and Vibro-acoustics in the PMSM with SVPWM. *IET Power Electron.* **2020**, *13*, 1033–1040. [CrossRef]
17. Divyam; Saxena, A.; Singh, B.; Rai, J.N. Comparative Analysis of PWM Techniques and SVPWM Operated V/f Control of Induction Motor Having Different Power Ratings. In Proceedings of the 2020 5th International Conference on Communication and Electronics Systems (ICCES), Coimbatore, India, 10–12 June 2020; IEEE: Piscataway, NJ, USA, 2020; pp. 6–11.

18. Bouyahi, H.; Ben Smida, K.; Khedher, A. Experimental Study of PWM Strategy Effect on Acoustic Noise Generated by Inverter-fed Induction Machine. *Int. Trans. Electr. Energy Syst.* **2020**, *30*, e12249. [CrossRef]

19. Shayestehfard, A.; Mekhilef, S.; Mokhlis, H. Modified Scalar Discontinuous Pulse-width Modulation Method for Two-level Three-wire Voltage Source Inverters under Unbalanced and Distorted Conditions. *IET Power Electron.* **2015**, *8*, 1339–1348. [CrossRef]

20. Liu, F.; Xin, K.; Liu, Y. An Adaptive Discontinuous Pulse Width Modulation (DPWM) Method for Three Phase Inverter. In Proceedings of the 2017 IEEE Applied Power Electronics Conference and Exposition (APEC), Tampa, FL, USA, 26–30 March 2017; IEEE: Piscataway, NJ, USA, 2017; pp. 1467–1472.

21. Huang, Y.; Xu, Y.; Zhang, W.; Zou, J. Hybrid RPWM Technique Based on Modified SVPWM to Reduce the PWM Acoustic Noise. *IEEE Trans. Power Electron.* **2019**, *34*, 5667–5674. [CrossRef]

22. Pindoriya, R.M.; Rajpurohit, B.S.; Kumar, R. A Novel Application of Harmonics Spread Spectrum Technique for Acoustic Noise and Vibration Reduction of PMSM Drive. *IEEE Access* **2020**, *8*, 103273–103284. [CrossRef]

23. Sivarani, T.S.; Joseph, J.S.; Agees, K.C. Intensive Random Carrier Pulse Width Modulation for Induction Motor Drives Based on Hopping between Discrete Carrier Frequencies. *IET Power Electron.* **2016**, *9*, 417–426. [CrossRef]

24. Chen, K.; Xie, Y. Multiphase Optimal Injection PWM with Dual Carrier Frequency to Reduce Current THD. *IET Power Electron.* **2017**, *10*, 1061–1076. [CrossRef]

25. Lee, K.; Shen, G.; Yao, W.; Lu, Z. Performance Characterization of Random Pulse Width Modulation Algorithms in Industrial and Commercial Adjustable-Speed Drives. *IEEE Trans. Ind. Appl.* **2017**, *53*, 1078–1087. [CrossRef]

26. Trzynadlowski, A.M.; Blaabjerg, F.; Pedersen, J.K.; Kirlin, R.L.; Legowski, S. Random Pulse Width Modulation Techniques for Converter-Fed Drive Systems-a Review. *IEEE Trans. Ind. Appl.* **1994**, *30*, 1166–1175. [CrossRef]

27. Andersson, A.; Lennstrom, D.; Nykanen, A. Influence of Inverter Modulation Strategy on Electric Drive Efficiency and Perceived Sound Quality. *IEEE Trans. Transp. Electrif.* **2016**, *2*, 24–35. [CrossRef]

28. Bhavani, J.; Amarnath, J.; Subba Rayudu, D. Generalized PWM Algorithm for VSI Fed Induction Motor Drives Using the Only Sampled Reference Phase Voltages. In Proceedings of the 2012 IEEE 5th India International Conference on Power Electronics (IICPE), Delhi, India, 6–8 December 2012; IEEE: Piscataway, NJ, USA, 2012; pp. 1–5.

29. Liang, W.; Luk, P.C.-K.; Fei, W. Analytical Investigation of Sideband Electromagnetic Vibration in Integral-Slot PMSM Drive with SVPWM Technique. *IEEE Trans. Power Electron.* **2017**, *32*, 4785–4795. [CrossRef]

30. Qiu, Z.; Huang, X.; Ma, K.; Kong, Z.; Liu, X. Sideband Vibro-Acoustic Responses and Improvements with Different Pulsewidth Modulation Strategies in Permanent Magnet Synchronous Motor for Electric Vehicle. *IEEE J. Emerg. Sel. Topics Power Electron.* **2022**, *10*, 7098–7108. [CrossRef]

31. Wang, D.; Yang, W.; Yang, J.; Jiang, K.; Fu, Y. Research on Electromagnetic Vibration Characteristics of a Permanent Magnet Synchronous Motor Based on Multi-Physical Field Coupling. *Energies* **2023**, *16*, 3916. [CrossRef]

32. Lu, Y.; Li, J.; Qu, R.; Ye, D.; Lu, H.; Sun, J.; Ge, M.; Xu, H. Electromagnetic Force and Vibration Analysis of Permanent-Magnet-Assisted Synchronous Reluctance Machines. *IEEE Trans. Ind. Appl.* **2018**, *54*, 4246–4256. [CrossRef]